Micro-scale fracturing mechanisms in coal induced by adsorption of supercritical CO_2

Yihuai Zhang[1*], Zike Zhang[2], Mohammad Sarmadivaleh[1], Maxim Lebedev[3], Ahmed Barifcani[1], Hongyan Yu[4], Stefan Iglauer[1]

[1]*Department of Petroleum Engineering, Curtin University, 26 Dick Perry Avenue, 6151, Kensington, Australia*

[2]*Department of Petroleum Engineering, China University of Petroleum, Beijing, 102249, China*

[3]*Department of Exploration Geophysics, Curtin University, 26 Dick Perry Avenue, 6151, Kensington, Australia*

[4]*Department of Geology, Northwest University, Xi'an, 710069, China*

[*]corresponding author (yihuai.zhang@postgrad.curtin.edu.au)

Abstract

Coal bed methane production can be assisted by CO_2 injection. However, CO_2 adsorption in the coal matrix leads to a dramatic reduction in permeability and an associated change in microstructure caused by coal matrix swelling. Furthermore, it has been recently observed that the induced swelling stress fractures the unswelling (mineral) phase in laboratory investigations. However, the failure mechanisms are still not understood, and the way internal swelling stresses are generated is not clear. Thus, in this paper, we propose a new method which combines x-ray microtomography imaging, nanoindentation testing and DEM modeling with which we can predict the rock mechanical performance at micro scale. Indeed we successfully simulated such swelling processes inside a coal sample, including a simulation of the fracture mechanism of the mineral phase, and a quantification of the in-situ von Mises stresses generated by swelling. We conclude that our proposed method is an efficient way for analysis and prediction of coal microfracturing and the associated microscale rock mechanical behavior.

1.   Introduction

Coal bed methane (CBM) is an unconventional energy resource, which exists in coal mines and deep unmineable coal seams (Hamawand et al., 2013). Recently, due to the decline in conventional energy resources coupled with a globally increasing energy demand (Lior 2008), CBM has gained increasing popularity (Connell et al., 2011; Pillalamarry et al., 2011; Hamilton et al., 2015; Vishal et al., 2015). Furthermore, CBM can be enhanced (enhanced coal bed methane, ECBM), e.g. through CO_2 injection, which efficiently displaces CH_4 from the coal matrix (White et al., 2005; Saghafi 2010). However, CO_2 injection dramatically reduces the coal seam's permeability (Mazumder et al., 2006; Siriwardane et al., 2009; Anggara et al., 2016), which largely limits application of this technology. Mechanistically, cleats (the main flow conduits in coal) close due to coal matrix swelling induced by CO_2 adsorption (Shi and Durucan 2005; Wu et al., 2011; Zhang et al., 2016a; Liu and Rutqvist 2010; Espinoza et al., 2014) and it has recently been discovered that the swelling stress in the coal matrix can fracture the unswelling phase (i.e. inorganic mineral), (Zhang et al. 2016a). However, the detailed failure mechanisms and swelling stress quantification are still poorly understood due to only limited theoretical understanding of the micro-scale rock mechanical performance. It is thus of vital importance to further understand these mechanical changes in the coal so that advanced ECBM techniques can be developed.

The mechanical properties of small areas (up to nanoscale) on a material's surface can now be obtained by nanoindentation measurements; such method has for instance been applied to natural rock samples including sandstone, limestone, shale and coal (Zhu et al., 2009; Bobko et al., 2011; Lebedev et al., 2014; Manjunath and Nair, 2015; Vialle and Lebedev, 2015; Liu et al., 2016). Thus nanoindentation gives us a way to identify the mechanical properties of heterogeneous coal (note that coal consists of the organic coal base matrix, inorganic minerals and pores). These mechanical properties are essential input data into numerical models, which can predict the mechanical behavior of the whole (heterogeneous) material. Earlier studies considered the coal matrix as a homogenous elastic continuum (e.g. Izadi et al., 2011), which

2

61 obviously cannot capture the clearly heterogeneous character of the coal, and thus can only

62 provide rather biased predictions. To overcome this serious limitation we use discrete element

63 method (DEM) modelling (cp. Cundall and Strack, 1979; Wang et al., 2014; Zhang et al.,

64 2016e; Bai et al., 2016), where each material – coal matrix, mineral and void are assigned their

65 respective true and individual mechanical properties, and combine this with high resolution x-

66 ray micro-computed tomography (microCT) imaging, which can provide the detailed 3D

67 morphology of the coal (Zhang et al., 2016b, 2016c, 2016d; Jing et al., 2016; Mostaghimi et

68 al., 2017). Thus, in this paper, using this approach, we were able to quantify the swelling

69 stresses generated by supercritical CO_2 injection into coal, and to identify the failure

70 mechanisms occurring in the un-swelling phase.

71

2.   Methodology

2.1   Experimental work

74 A small cylindrical coal plug (5 mm diameter and 10 mm length) was cut from a heterogeneous

75 subbituminous medium rank coal block obtained from a coal seam at ~650m to 700m depth

76 (buried at Permian period) from Pingdingshan coal mine, China; the generalized stratigraphic

77 column is shown in Figure 1. The coal had a 54% (±2%) carbon content and a 36% (±1%)

78 volatile matter content (measured by Chinese Standard GB/T 212-2008 and DL/T 1030-2006;

79 Xu et al., 2016; Zhang et al., 2016d), additional properties are tabulated in Table 1.The

80 microstructure of the sample is shown in Figure 2, the coal matrix, cleats and mineral phase

81 can clearly be seen. The mineral was identified as calcite in SEM-EDS analysis. This plug was

82 mounted into a HPHT (high pressure – high temperature) x-ray transparent flow cell (core

83 holder), which was integrated into an in-situ microCT core flooding system (cp. Lebedev et al.,

84 2016; Zhang et al., 2016c, 2016d; Iglauer et al., 2011; Rahman et al. 2016). The plug was

85 vacuumed for 8 hours and subsequently more than 5000 PV (pore volumes) of $scCO_2$ were

86 injected at typical reservoir conditions (confining pressure = 15 MPa, pore pressure = 10 MPa,

87 temperature = 323 K (50°C), Pentland et al., 2011; Iglauer et al., 2011). The coal plug was

88 imaged at high resolution (voxel size = 3.43 µm) with an Xradia VersaXRM instrument in 3D,

89 before and after $scCO_2$ flooding. Indeed the sample's micro-morphology changed significantly,

90 micro cleats/fractures in the coal matrix closed due to swelling induced by $scCO_2$ adsorption

91 (cp. 3 and 5 in Figure 3), and new fractures appeared in the un-swelling calcite phase (cp. 1, 2

92   and 4 in Figure 3); see Zhang et al., (2016b) for the details of this in-situ microCT scCO$_2$ core

93   flooding experiment.

Depth (m)	Graphic	Explanation	Thickness
		clay, mud, sand with gravel and calcrete	31
		Sandstone	161
		Sandstone	23
		clay, mud, silty sandstone	98
		Sand and mud interlayer	187
		mudstone	46
		Sand and mud interlayer	73
		Mudstone	16
		clay, mud, silty sandstone	33
		Coal	14
		Sand and mud interlayer	59
		clay, mud, silty sandstone	24
		Coal	10
		clay, mud, silty sandstone	75
		clay, mud, silty sandstone	80
		Coal	24
		Limestone	>50

94

95 Figure 1. The generalized stratigraphic column of the Pingdingshan coal mine from which the
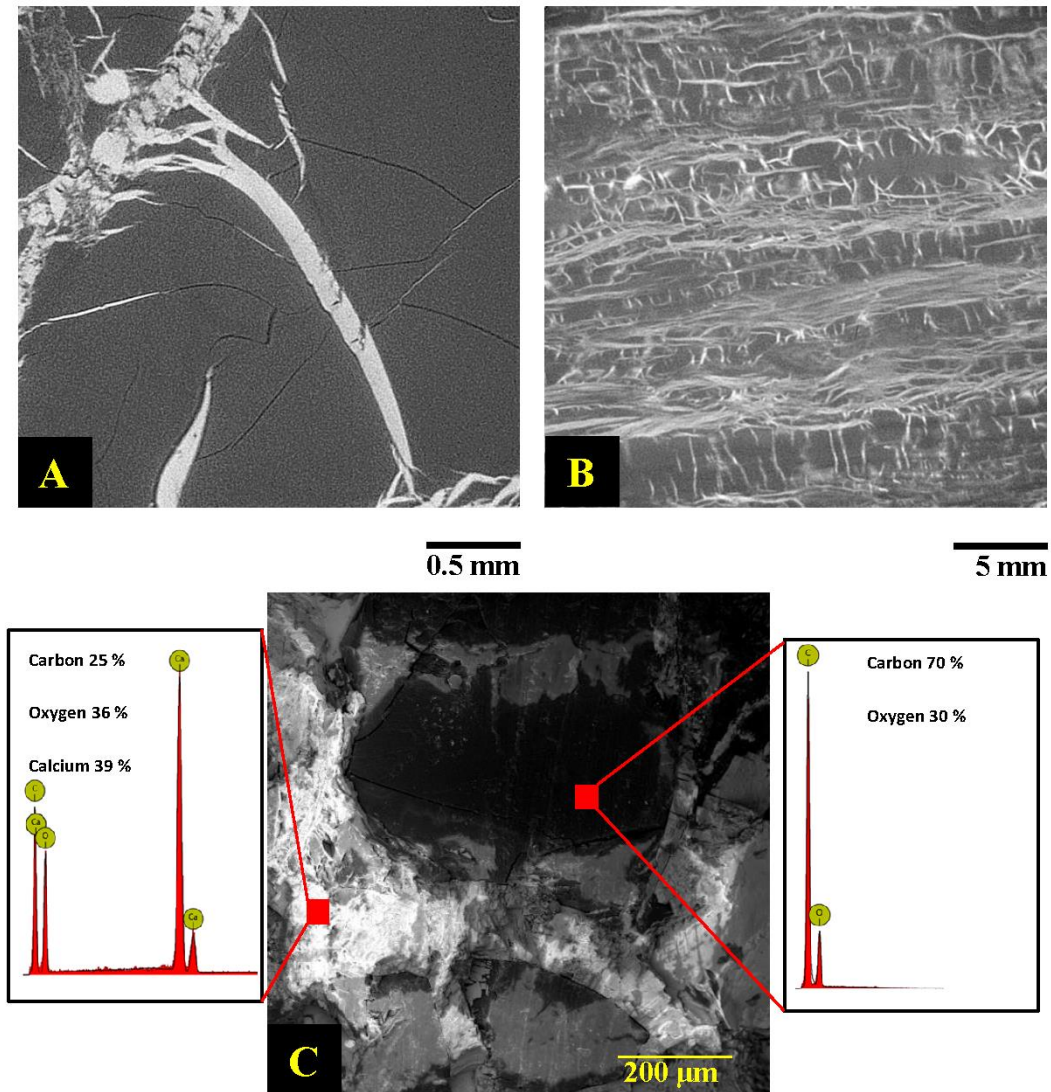
96 coal sample was obtained.

97

98 Table 1: Physical properties of the coal studied (Xu et al. 2016; Zhang et al. 2016d).

| M (%)	V (%)	A (%)	C_f (%)	E (GPa)	υ	ρ (g/cm^3)
6.9	36.0	4.2	54.0	2.6	0.3	1.35

99 Note: M is the moisture content; V is the volatile matter; A is the ash yield; C_f is the fixed carbon content; E is

100 Young's Modulus; υ is Poission's ratio; and ρ is the bulk density.

101

Figure 2. The micro structure of the unflooded coal sample; (A), (B): 2D microCT slices through the greyscale image; (A) 3.43 µm voxel size; (B) 33.7 µm voxel size, grey is coal matrix, black is void space, and white is calcite; (C) SEM image of the coal and associated EDS spectra; calcite is white and coal matrix is black/dark grey.

107
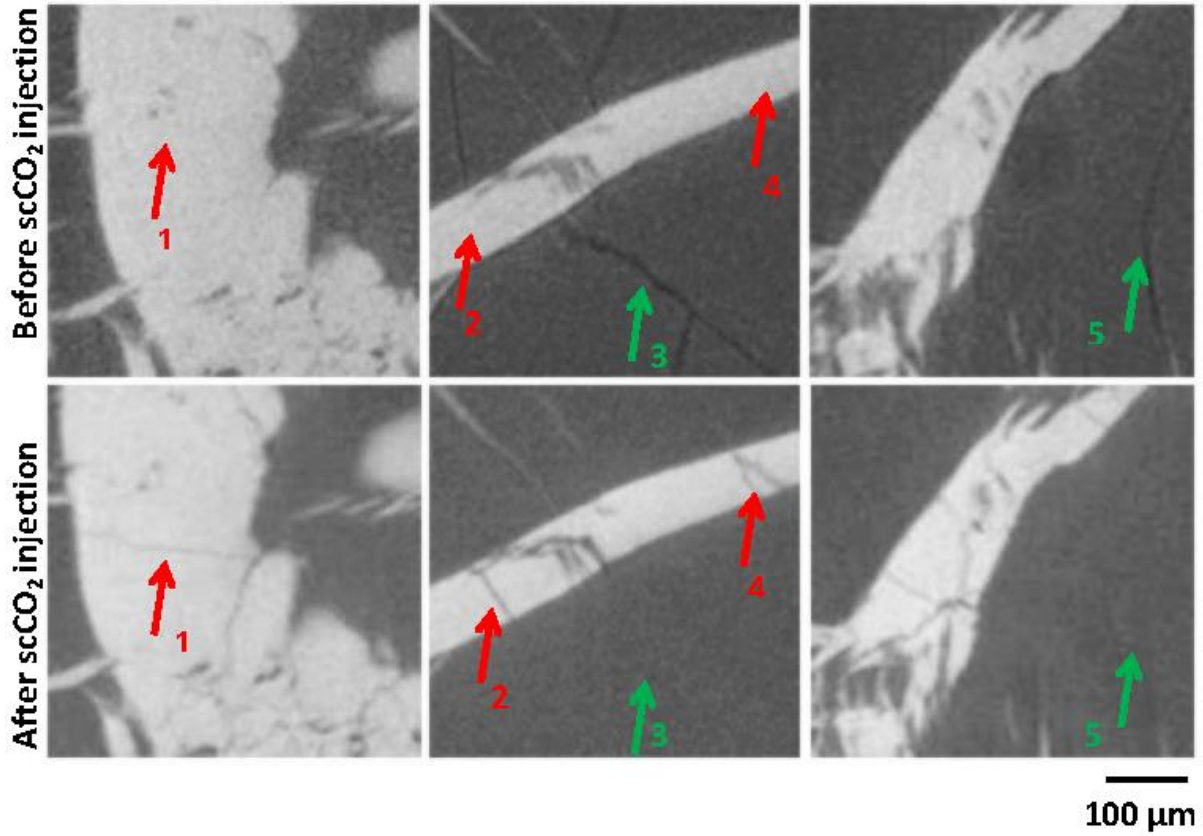
Figure 3. 2D microCT slices through the coal sample before and after scCO$_2$ injection (3.43 µm resolution); new fractures appeared in the calcite after flooding: 1, 2 and 4; the original micro cleats in the coal matrix closed after flooding: 3 and 5.

3. The stress-strain method

Initially we estimated the swelling stress via the traditional stress-strain method using the volume fractions measured (i.e. strains measured) on the microCT images, Table 2 (note that the volume strain ε = (the volume difference before and after CO$_2$ flooding) / (original volume). Negative values represent compression, while positive values represent expansion.

What is more, in an elastic 3D coordinate system, ε has following relation with Young's modulus (E), stress (σ), and Poisson's ratio (v), e.g. Fjar et al., 2008; Ahmed and Meehan (2016):

$$\begin{cases} \varepsilon_x = \frac{1}{E} \left[\sigma_x - v(\sigma_y + \sigma_z) \right] \\ \varepsilon_y = \frac{1}{E} \left[\sigma_y - v(\sigma_x + \sigma_z) \right] \\ \varepsilon_z = \frac{1}{E} \left[\sigma_z - v(\sigma_x + \sigma_y) \right] \end{cases} \tag{1}$$

7

120   Based on the former stress-strain studies on coal (cp. Seidle et al., 1992; Sheorey, 1994; Tajduś,

121   2009; Liu and Rutqvist, 2010; Espinoza et al., 2013), we assumed that the coal was under

122   isotropic elastic and hydrostatic conditions, thus

123     $\sigma_x = \sigma_y = \sigma_z$ (2)

124   It follows for the volume matrix strain (ε_v):

125     $\varepsilon_v = 3\varepsilon_x = 3\frac{1}{E}\left[\sigma_x - v2\sigma_x\right]$ (3)

126   As the strain (ε) is equal to the volume matrix strain (ε_v) / 3, thus

127     $\varepsilon = \frac{1}{E}\sigma(1 - 2v)$ (4)

128   So,

129     $\sigma = \frac{E\varepsilon}{1-2v}$ (5)

130   Furthermore, the effective stress (σ_e) can be described as a function of internal swelling stress

131   (σ_s), Liu and Rutqvist (2010):

132     $\sigma_e = \sigma_t - \alpha P + \sigma_s$ (6)

133   Thus before scCO$_2$ injection (without swelling effect), the effective stress for the material can

134   be described as

135     $\sigma_{e1} = \sigma_{t1} - \alpha P_1$ (7)

136   After scCO$_2$ injection (with swelling effect)

137     $\sigma_{e2} = \sigma_{t2} - \alpha P_2 + \sigma_s$ (8)

138   and the differential effective stress (before and after CO$_2$ adsorption) σ (generated by the strain

139   change) is thus:

140     $\sigma = \sigma_{e2} - \sigma_{e1} = \sigma_{t2} - \alpha P_2 + \sigma_s - \sigma_{t1} + \alpha P_1 = \frac{E\varepsilon}{1-2v}$ (9)

141   Thus the internal swelling stress (σ_s) can be obtained by

142     $\sigma_s = \frac{E\varepsilon}{1-2v} - \sigma_{t2} + \alpha P_2 + \sigma_{t1} - \alpha P_1$ (10)

143   Where σ_{t2} is the overburden (confining) pressure (15 MPa), P_2 is the pore pressure (10 MPa)

144   for the second microCT scan, σ_{t1} is 5 MPa, P_1 is 0 MPa for the first microCT scan, and α is

145   Biot's coefficient. Based on previous studies (e.g. Gray, 1987; Liu and Rutqvist, 2010), we set

146   Biot's coefficient $\alpha = 1$. For the coal matrix, we set a Young's modulus (E) of 2 GPa and a

147   Poisson's ratio (v) of 0.15 (an estimated value from an ultrasonic test on a sister coal plug,

148   measured with a RIGOL DS4022 instrument at 1 MHz frequency). After inputting the data into

149   equation (10), we obtained an internal swelling stress value of 20.52 MPa. However, the

150   shortcoming of this stress-strain prediction was significant; the result cannot reflect the

151   swelling progress which is dynamic (different swelling degrees induce different internal

152   swelling stresses), and the assumption of isotropic elasticity is a strong simplification when

153   modelling highly heterogeneous coal. Most importantly, this method cannot answer the

154   questions about the failure mechanisms occurring in the mineral phase. Thus, further numerical

155   modelling is required (see DEM simulations below).

156

157   Table 2: Volumetric and strain data for each phase before and after CO_2 flooding.

Phases	The volume before scCO$_2$ injection [$10^6 \mu m^3$]	The volume after scCO$_2$ injection [$10^6 \mu m^3$]	Volume matrix Strain (ε_v)	Strain (ε)
Void (Micro cleats/fractures)	26.17	0	-1	-1
Coal matrix	5500.08	5618.61	0.022	0.007
Calcite mineral	2171.02	2078.66	-0.043	-0.014
Total	7697.270	7697.27	0	0

158

4.   Discrete Element Method (DEM) simulation

160   The Discrete Element Method (DEM) has become a powerful numerical tool for analyzing the

161   dynamic mechanical behavior of complex objects (Cundall and Strack, 1979; Scholtès and

162 Donzé, 2012). Precisely, DEM models objects as an assembly of interacting particles, and the

163 key advantage of DEM is that specific attributes (features, bonds, contacts, frictions and

164 boundary conditions) can be assigned to each particle (and thus each material) simultaneously.

165 We used the popular DEM built-in software – Particle Flow Code (PFC2D) in this study. In

166 PFC2D, the DEM simulations are based on Newton's second law and the force-displacement

167 law at particle contacts. While the force-displacement law determines the contact force exerted

168 on each particle (these forces arise from the relative motion of the particles to each other);

169 Newton's second law determines the motion for each particle (which arise from the contact

170 and body forces acting upon the particle), Cundall and Strack (1999). The constitutive behavior

171 of the material is simulated by stiffness model, slip model and bonding model. The stiffness

172 model provides the elastic relationship between the displacement and contact force, and the

173 slip model describes the relationship between normal and shear contact force when the

174 contacted particles slip in relation to each other; and the bonding model limits the total shear

175 and normal forces in the contact areas (Cundall and Strack, 1999; Sarmadivaleh, 2012;

176 Hashemi et al., 2014; Bewick et al., 2014; Zhang et al., 2016e; Zhou et al., 2016; Jiang et al.,

177 2016). Here we used a small particle size (less than 6 µm) to simulate the coal matrix and

178 calcite mineral at micro-scale; and the effective stress applied in the true experiment has been

179 added via a boundary condition set, see below. Furthermore, the contact bond model (see

180 Potyondy and Cundall, 2004) was used in our simulation; and most importantly, the coal

181 swelling effect was modelled by continuously increasing the volume of the coal matrix particles.

182 Six simulations were performed (A – E), Figure 4. Each simulation used a high resolution 2D

183 microCT slice acquired experimentally (thus different micro-morphologies were tested,

184 Figures 4 and 5) to provide realistic geometrical input data. The simulations covered different

185 areal sizes: A and B were 0.4 mm × 0.4 mm, C was 0.85 mm × 0.85 mm, D and E were 1.37

186 mm × 1.37 mm. The number of particles in examples A, C and D were set to ~7000, in example

187 B to ~20000 and in example E both particle numbers were tested (i.e. both, ~7000 in E2, and

188 ~20000 in E1). The volume of each particle in the coal matrix was increased until a total volume

189 (of each particle) increase of 1% was realized (which simulated the coal matrix swelling during

190 scCO$_2$ injection). A servo-control mode boundary condition with 5 MPa effective stress was

191 used to mimic the experimental conditions (where 5 MPa effective stress was applied, see

192 above). Other input parameters are summarized in Table 3. To obtain reasonable shear/normal

193 bond strengths in the DEM simulations, calibration simulations were run on example E for

194 different bond strengths (ranging from 1 MPa to 110MPa), see Figure 6.

195   These calibration simulations used model E and a 1 % total coal particle volume swelling factor.
196   Thus after comparing the computed fracture morphologies with the experimental microCT
197   tomography results, we chose 50 ± 5 MPa (normally distributed) for the shear/normal bond
198   strengths in all DEM simulations. Note that the bond strength input did not affect the final
199   internal swelling stress output, and the maximal von Mises stresses predicted for all cases (at
200   1 % particle swelling rate) were similar, around 20 MPa.
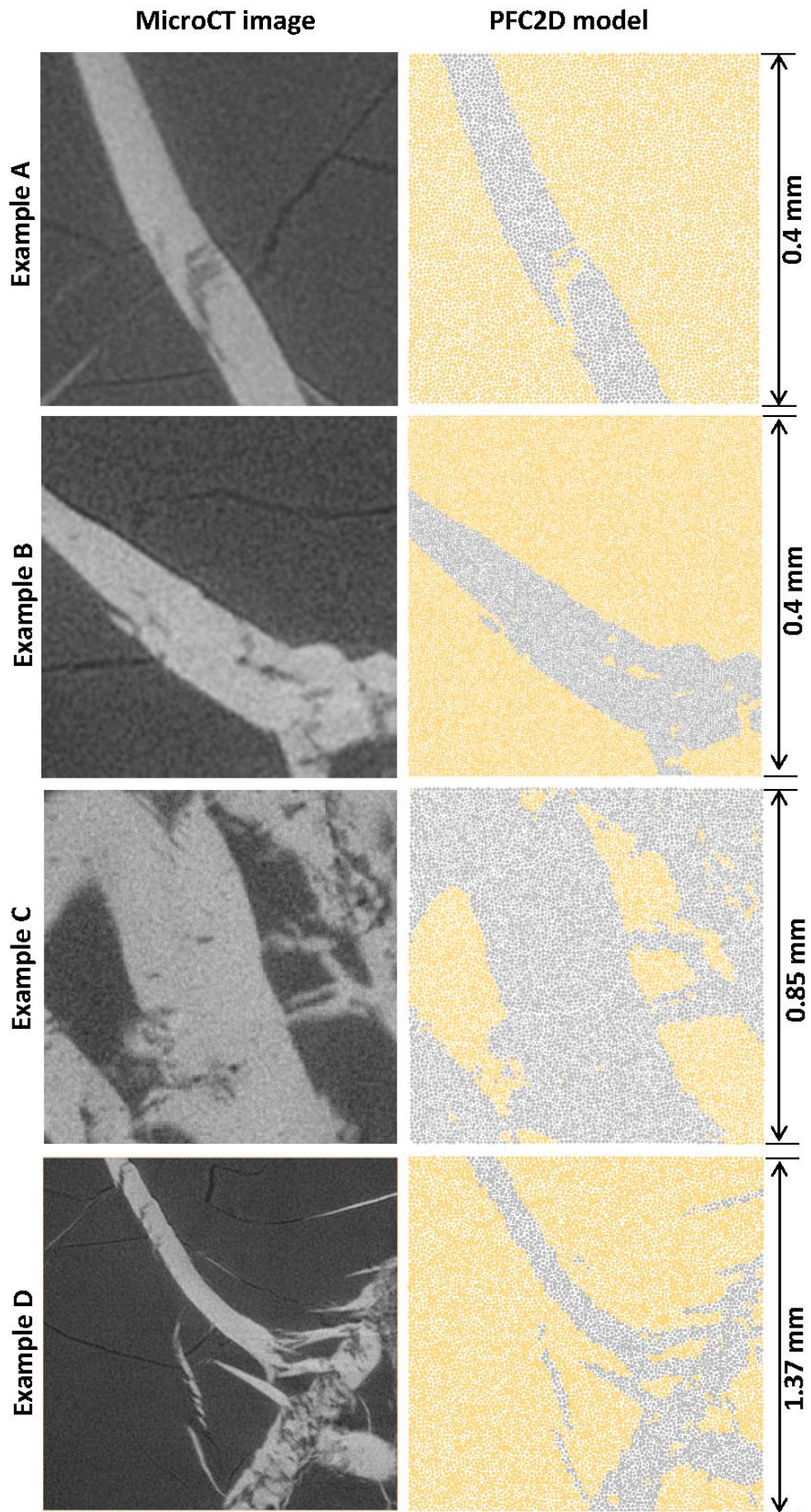
201

202

203

204   Table 3. Particle properties used in the DEM simulations.

| Input property	Value
Particle density (coal matrix)	1052 kg/m^3
Particle density (calcite mineral)	2000 kg/m^3
Particle radius	6 µm to 9µm (evenly distributed)
Friction coefficient	0.5
Shear Bond strength[*]	50 ± 5 MPa (normally distributed)
Normal Bond strength[*]	50 ± 5 MPa (normally distributed)
Young's modulus (coal matrix)[#]	1 GPa and 8 GPa (normally distributed)
Young's modulus (calcite mineral)[#]	18 GPa

205   [*]The Bond strength was chosen after conducting calibration simulations, see text for details.

206   [#]The Young's moduli were obtained from the nanoindentation tests, see text for details.

	MicroCT image	PFC2D model	

Example A — 0.4 mm

Example B — 0.4 mm

Example C — 0.85 mm

Example D — 1.37 mm

208   Figure 4. PFC2D models and associated microCT images, examples A – D; A, C and D used

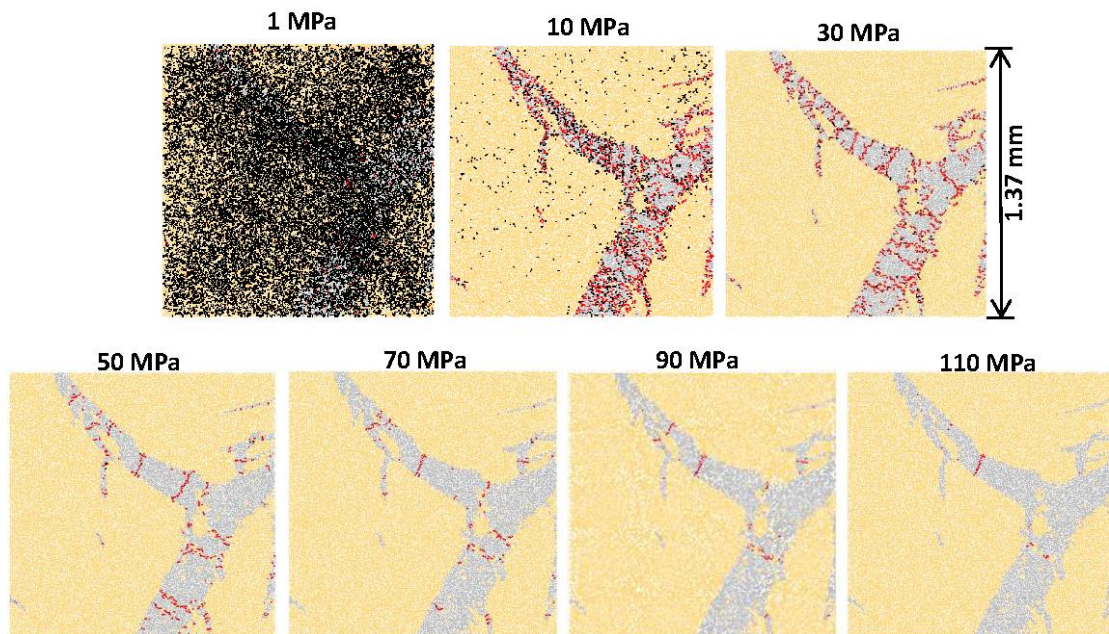209   ~7000 particles, and B ~20000 particles.

210
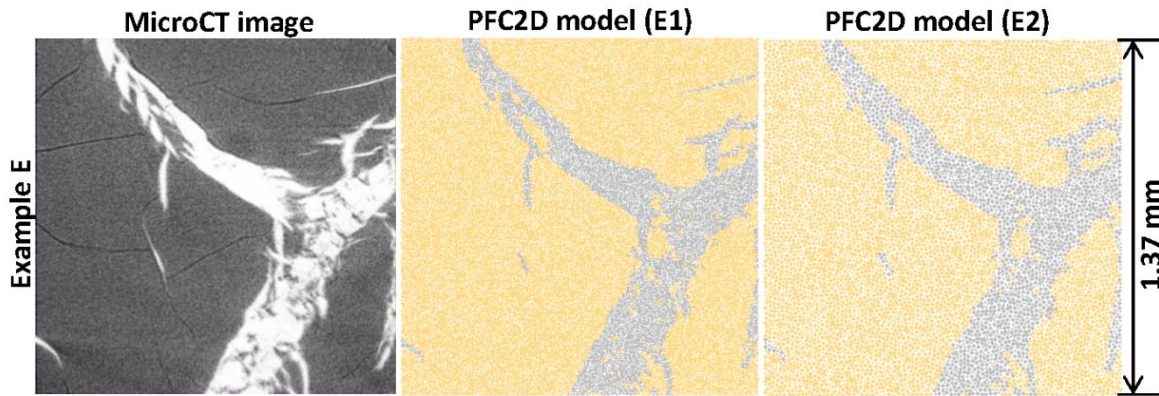
211

212   Figure 5. The PFC2D models with the associated microCT image, example E: E1 used ~20000

213   particles; and E2 ~7000 particles.

214

215

216   Figure 6. Calibration simulations for setting the bond strength. Simulations for 1 MPa to 110

217   MPa bond strength are shown, for a 1 % coal matrix swelling factor.

5. Nanoindentation testing

The IBIS nanoindentation system and Berkovich nano-indenter were chosen for the nanoindentation tests, Figure 7. A cuboid coal sample ($l \times w \times h = 5$ mm $\times$ 5 mm $\times$ 2 mm) was cut and carefully polished, and mounted on the objective stage. Subsequently the penetration depth (h) – loading/unloading force (P) curves were measured for each test point. Specifically 625 data points on a symmetric 25×25 grid ($240\,\mu$m $\times 240\,\mu$m spacing) were measured. The maxim loading force was set to 4 mN (which is smaller than the one used in former studies on other natural rocks, Lebedev et al., 2014; Vialle and Lebedev, 2015; Zhang et al., 2016a) due to the brittle and soft nature of the coal sample. Finally, the indentation modulus (M) was obtained from the measured P-h curves, equation 8 (Fischer-Cripps, 2004):

$$M = \frac{1}{2} \frac{\sqrt{\pi}}{\sqrt{A}} \frac{dP}{dh} \tag{11}$$

where A is the contact area, and dP / dh was measured from several unloading curves at maximum applied force P_{max} and maximum penetration depth h_{max}. For an isotropic material Young's modulus E and Poisson's ratio v can then be related to M as:

$$M = \frac{E}{1-v^2} \tag{12}$$

Furthermore, E can be approximated via (Fischer-Cripps, 2004; Lebedev et al., 2014):

$$0.75\, M \leq E \leq M \tag{13}$$

when the material's Poisson's ratio ranges from 0 to 0.5 (the Poisson's ratio is less than 0.5 for most natural materials, we estimated $v = 0.15$ from the bulk volume ultrasonic test and $v \approx 0.3$ for coal was reported by Wang et al., 2014),

The nanoindentation results are presented in Figure 7. It is clear from this data that the indentation modulus of the mineral phase (always larger than 15 GPa) was significantly higher than that of the coal matrix. Thus, for the DEM input, the E for the coal matrix was set to 1 GPa to 8 GPa (normally distributed) recall that coal is highly heterogeneous, and 18 GPa for the calcite phase.

245

246
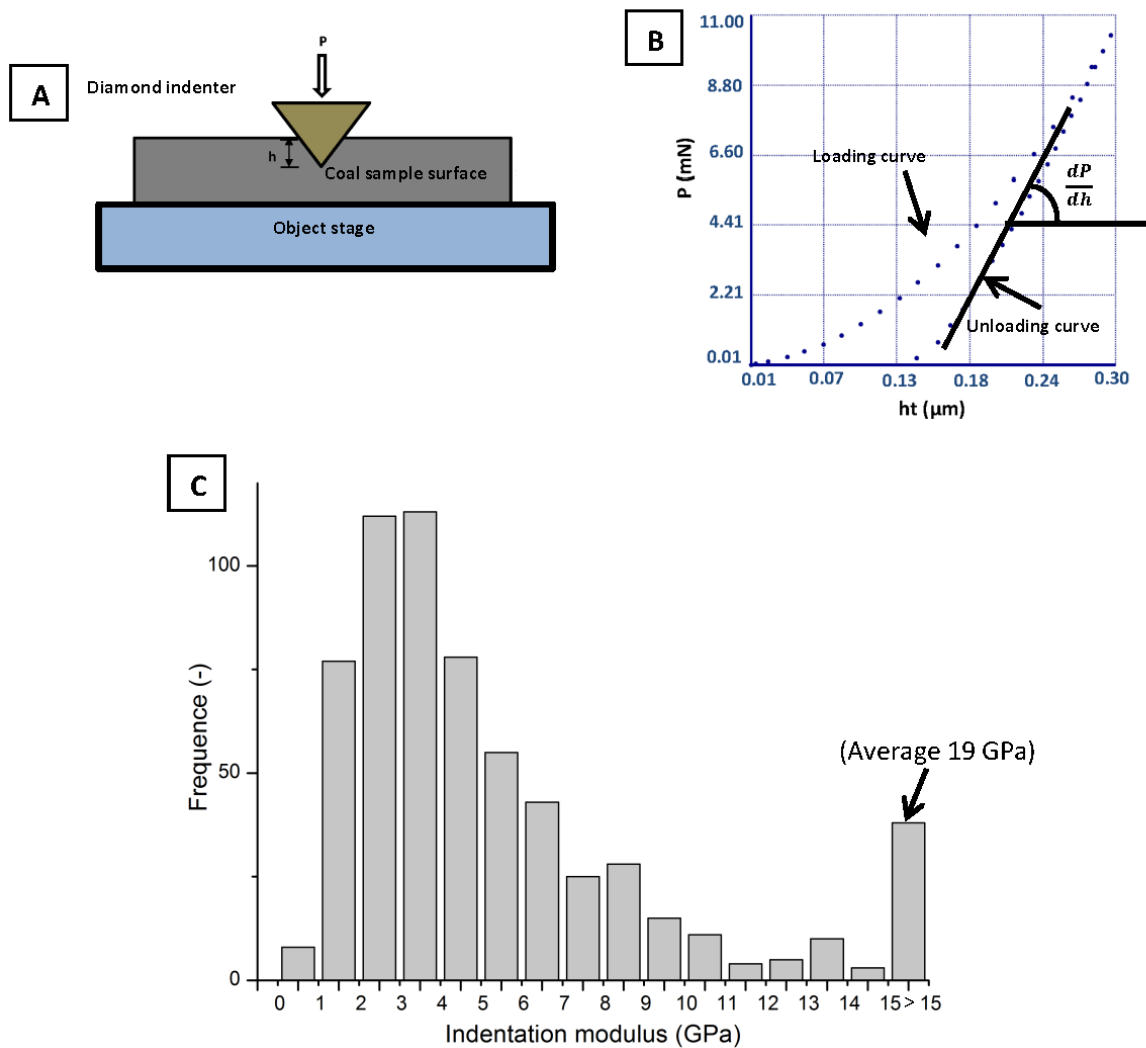
Figure 7. (A) Schematic of the nanoindentation experiment, the indenter penetrates into the sample during loading; (B) a typical loading - unloading curve for the quartz calibration sample (A Young's modulus of 72.5 GPa, a Poisson's ration of 0.17, and an indentation modulus of 74.5 GPa were measured) where the h (µm) is the indentation depth and P (mN) is the indentation force; (C) indentation moduli (GPa) measured on the coal sample.

252

6.   Results and discussion

The DEM simulations successfully predicted the change in coal microstructure caused by coal matrix swelling, which again was induced by scCO$_2$ injection (see Figures 8 and 9). Clearly cracks appeared in the mineral phase when the coal matrix volume increased by 1 %, consistent

257 with the experimental microCT observations (cp. Figure 3). Most failures in the calcite mineral

258 phase were identified as tensile failures (red colored cracks in Figures 8 and 9) these appeared

259 during the coal matrix swelling. We were furthermore able to compute the in-situ stresses, c.p.

260 the von Mises stress map in Figure 8 and Figure 9). Note that the von Mises stress K is defined

261 by

262 $$\sigma_1^2 - \sigma_1\sigma_2 + \sigma_2^2 = 3K^2 \tag{14}$$

263 and a K map can describe the in-situ stress exerted on each particle in the model. Clearly these

264 stress fields were highly anisotropic, and maximum effective stresses concentrated on the

265 mineral surface in most cases (Example A, B, D and E). The von Mises stresses continuously

266 increased with increasing coal matrix swelling until failure (i.e. until the mineral was fractured).

267 During failure, the swelling stresses generated were released, and the von Mises stress

268 decreased again.

269 Furthermore, the number of particles in the simulation had no significant influence on the in-

270 situ stresses (compare simulations E1 and E2 in Figure 9), although a larger particle number

271 predicted a more realistic fracture morphology. Moreover, the volume fraction and morphology

272 of the mineral was identified as the main factor determining the highest in-situ stresses; see

273 example C (where the coal matrix volume fraction was only 20 %) in Figure 8; note that in this

274 example, the highest in-situ effective stresses were located in the coal matrix, but not on the

275 mineral surface, contrary to the behavior of the other examples. This can be explained by a

276 morphological feature; the coal matrix was fully enclosed and trapped by the mineral phase,

277 thus the generated stresses could not be released until all surrounding minerals failed. However,

278 the mineral was less likely to fail as it had a much higher volume fraction than the coal matrix,

279 and its Young's modulus was significantly higher than that of the coal matrix; thus abnormally

280 high stresses appeared inside the coal.

281 Finally the relationship between maximum von Mises stress (MPa), in in-situ von Mises stress

282 map, and swelling percentage could be calculated, cp. Figure 10. Thus, the dynamic swelling

283 stress (in-situ effective stress minus the original effective stress) could be obtained: the swelling

284 stress in the normal areas (with an approximately 70 % coal matrix volume fraction) reached

285 up to 20 MPa, while they reached more than 35 MPa in some areas where the coal matrix was

286 enclosed by the mineral phase. In a field scale CO_2-ECBM project, such abnormally high

287 swelling stresses (caused by CO_2 injection) can result in a series of problems such as well

288 borehole instabilities and/or fault re-activation (Karacan et al., 2011; Tu et al., 2016; Zhai et

289 al., 2016). These effects should be analyzed further as they pose a significant geohazard.

290
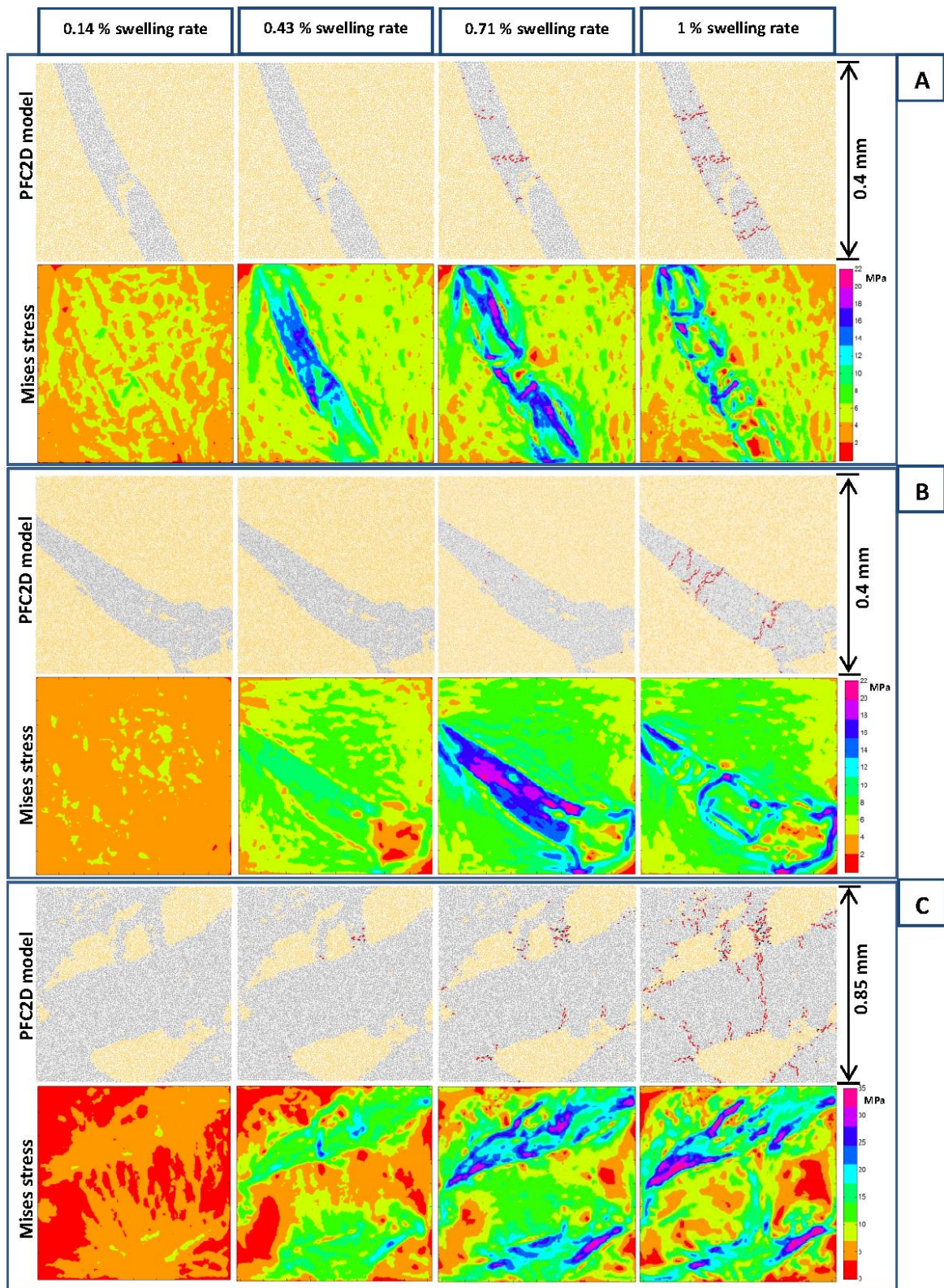
Figure 8. Fractures development due to scCO$_2$ injection predicted via DEM. The in-situ mises stress maps are shown in color below the PFC models; (A) example A; (B) example B; and (C) is example C. Note: the red colored cracks indicate tensile failures and the black colored shear failures.
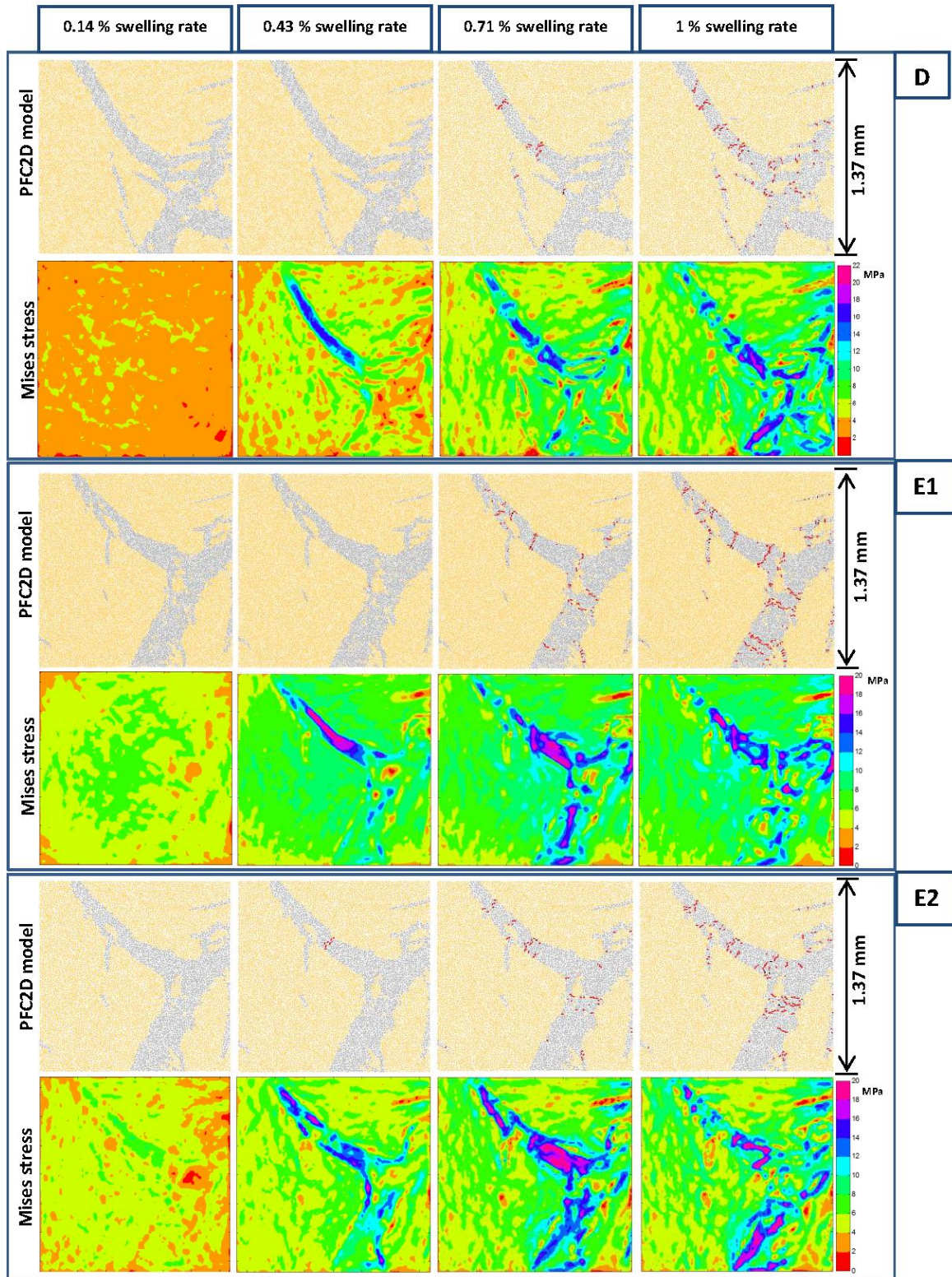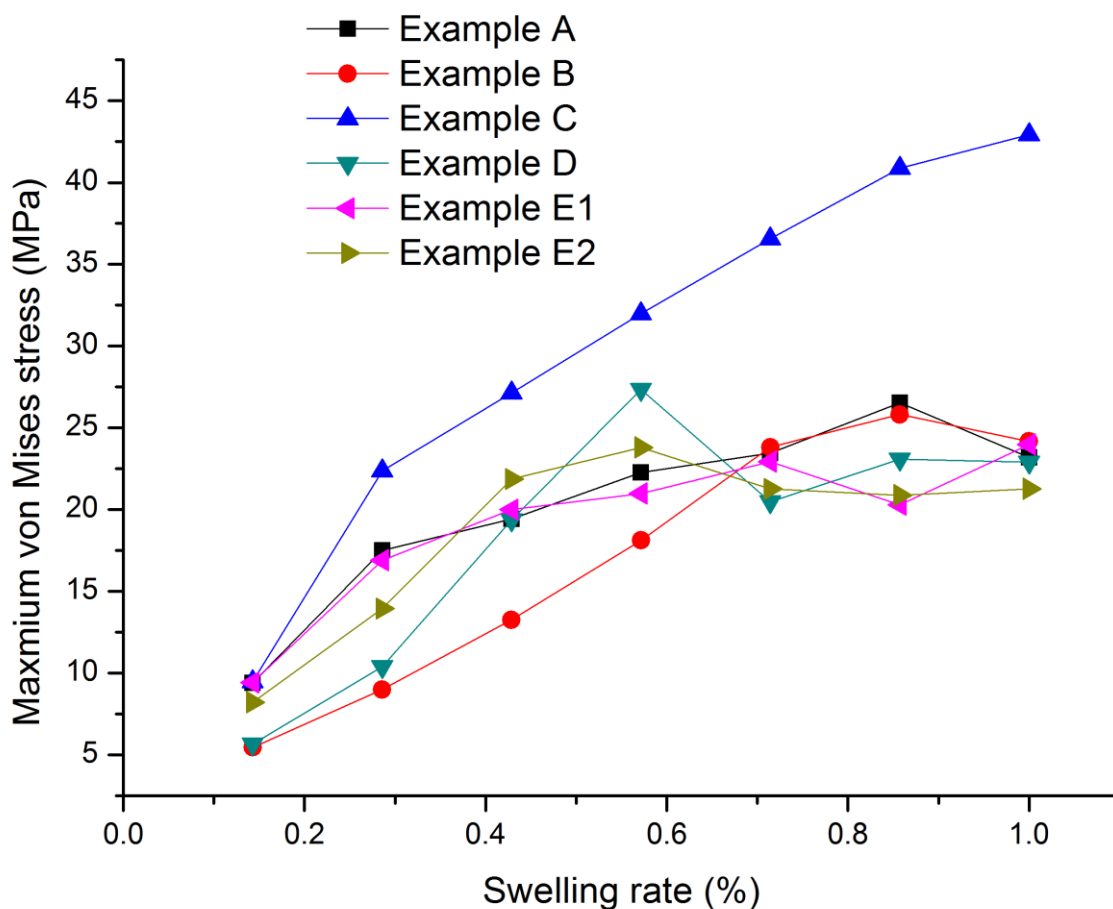
Figure 9. Fractures development due to scCO$_2$ injection predicted via DEM. The in-situ mises stress maps are shown in color below the PFC models; (D) example D; (E1) example E1; and

298 (E2) is example E2. Note: the red colored cracks indicate tensile failures and the black
299 colored shear failures.

300

301 Figure 10. The relationship between maximum von Mises stress (from in-situ von Mises
302 stress map, Figures 8 and 9) and swelling rate (%).

303

7. Conclusions

305 CO_2 can be injected into coal seams to enhance methane production (White et al., 2005; Saghafi
306 2010); however, the resulting coal matrix swelling effect leads to coal cleat closure and a
307 dramatic permeability reduction (Karacan 2003; Zhang et al., 2016f); furthermore, it has been
308 recently observed that the unswelling phase fractured due to the induced swelling stresses
309 (Zhang et al., 2016b). However, how precisely such swelling stresses are generated and the
310 associated failure mechanisms in the unswelling phase are not fully understood. Thus, in this
311 paper, we developed a novel microscale discrete element method (DEM) which combines x-

312   ray microCT tomography imaging and nanoindentation measurements to predict such

313   microscale rock mechanical performance.

314   These DEM simulations were run on five test samples where different geometrical

315   morphologies were examined (the microCT images provided this input). The DEM models

316   successfully simulated the swelling process and predicted failure morphologies in the mineral

317   phase consistent with the microCT observations. Based on the simulation results, we conclude

318   that the mineral phase shows tensile failure due to compression caused by coal matrix swelling.

319   The von Mises stresses were quantified, and the maximum coal swelling stresses reached more

320   than 35 MPa in areas which were fully enclosed by (unswelling) mineral. Such abnormally

321   high stresses pose a geohazard risk in CO_2-ECBM projects.

322

323

330

331

References

333   Ahmed, U., Meehan, D.N., 2016. Unconventional oil and gas resources: exploitation and development.
334   CRC Press.

336   Anggara, F., Sasaki, K. and Sugai, Y., 2016. The correlation between coal swelling and permeability
337   during CO 2 sequestration: A case study using Kushiro low rank coals. International Journal of Coal
338   Geology 166 62-70.

340   Bai, Q.-S., Tu, S.-H., Zhang, C., Zhu, D., 2016. Discrete element modeling of progressive failure in a wide
341   coal roadway from water-rich roofs. International Journal of Coal Geology 167, 215-229.

343   Bewick, R., Kaiser, P., Bawden, W., Bahrani, N., 2014. DEM simulation of direct shear: 1. Rupture under
344   constant normal stress boundary conditions. Rock Mechanics and Rock Engineering 47, 1647-1671.

345

346 Bobko, C.P., Gathier, B., Ortega, J.A., Ulm, F.J., Borges, L., Abousleiman, Y.N., 2011. The nanogranular
347 origin of friction and cohesion in shale—a strength homogenization approach to interpretation of
348 nanoindentation results. International Journal for Numerical and Analytical Methods in Geomechanics
349 35, 1854-1876.

350

351 Cundall, P.A., Strack, O.D., 1979. A discrete numerical model for granular assemblies. Geotechnique
352 29, 47-65.

353

354 Cundall, P., Strack, O., 1999. Particle flow code in 2 dimensions. Itasca consulting group, Inc.

355

356 Connell, L.D., Sander, R., Pan, Z., Camilleri, M. and Heryanto, D., 2011. History matching of enhanced
357 coal bed methane laboratory core flood tests. International Journal of Coal Geology 87(2), 128-138.

358

359 Espinoza, D., Vandamme, M., Dangla, P., Pereira, J.M., Vidal‐Gilbert, S., 2013. A transverse isotropic
360 model for microporous solids: Application to coal matrix adsorption and swelling. Journal of
361 Geophysical Research: Solid Earth 118, 6113-6123.

362

363 Espinoza, D.N., Vandamme, M., Pereira, J.M., Dangla, P. and Vidal-Gilbert, S., 2014. Measurement and
364 modeling of adsorptive–poromechanical properties of bituminous coal cores exposed to CO_2:
365 Adsorption, swelling strains, swelling stresses and impact on fracture permeability. International
366 Journal of Coal Geology, 134, 80-95.

367

368 Fischer-Cripps, A., 2004. Nanoindentation Springer. New York.

369

370 Fjar, E., Holt, R.M., Raaen, A.M., Risnes, R. and Horsrud, P., 2008. Petroleum related rock mechanics
371 (Vol. 53). Elsevier.

372

373 Gray, I., 1987. Reservoir engineering in coal seams: Part 1-The physical process of gas storage and
374 movement in coal seams. SPE Reservoir Engineering 2, 28-34.

375

376 Hamawand, I., Yusaf, T. and Hamawand, S.G., 2013. Coal seam gas and associated water: a review
377 paper. Renewable and Sustainable Energy Reviews 22, 550-560.

378

379 Hamilton, S.K., Golding, S.D., Baublys, K.A. and Esterle, J.S., 2015. Conceptual exploration targeting for
380 microbially enhanced coal bed methane (MECoM) in the Walloon Subgroup, eastern Surat Basin,
381 Australia. International Journal of Coal Geology 138, 68-82.

382

383 Hashemi, S., Momeni, A., Melkoumian, N., 2014. Investigation of borehole stability in poorly cemented
384 granular formations by discrete element method. Journal of Petroleum Science and Engineering 113,
385 23-35.

386

387 Iglauer, S., Paluszny, A., Pentland, C.H., Blunt, M.J., 2011. Residual CO_2 imaged with X‐ray micro‐
388 tomography. Geophysical Research Letters 38.

389

390 Izadi, G., Wang, S., Elsworth, D., Liu, J., Wu, Y., Pone, D., 2011. Permeability evolution of fluid-
391 infiltrated coal containing discrete fractures. International Journal of Coal Geology 85, 202-211.

392

393 Jiang, M., Fu, C., Cui, L., Shen, Z., Zhu, F., 2016. DEM simulations of methane hydrate exploitation by
394 thermal recovery and depressurization methods. Computers and Geotechnics.

395

396   Jing, Y., Armstrong, R.T., Ramandi, H.L. and Mostaghimi, P., 2016. Coal cleat reconstruction using
397   micro-computed tomography imaging. Fuel 181, 286-299.
398
399   Karacan, C.Ö., Ruiz, F.A., Cotè, M. and Phipps, S., 2011. Coal mine methane: a review of capture and
400   utilization practices with benefits to mining safety and to greenhouse gas reduction. International
401   Journal of Coal Geology 86(2), 121-156.
402
403   Karacan, C.Ö., 2003. Heterogeneous sorption and swelling in a confined and stressed coal during CO_2
404   injection. Energy & Fuels 17(6), 1595-1608.
405
406   Lebedev, M., Wilson, M.E., Mikhaltsevitch, V., 2014. An experimental study of solid matrix weakening
407   in water‑saturated Savonnières limestone. Geophysical Prospecting 62, 1253-1265.
408
409   Lior, N., 2008. Energy resources and use: the present situation and possible paths to the future. Energy
410   33(6), 842-857.
411
412   Liu, H.-H., Rutqvist, J., 2010. A new coal-permeability model: internal swelling stress and fracture–
413   matrix interaction. Transport in Porous Media 82, 157-171.
414
415   Liu, K., Ostadhassan, M. and Bubach, B., 2016. Applications of nano-indentation methods to estimate
416   nanoscale mechanical properties of shale reservoir rocks. Journal of Natural Gas Science and
417   Engineering, 35, 1310-1319.
418
418   Manjunath, G.L. and Nair, R.R., 2015. Implications of the 3D micro scale coal characteristics along with
419   Raman stress mapping of the scratch tracks. International Journal of Coal Geology, 141, 13-22.
420
421   Mazumder, S., Karnik, A.A. and Wolf, K.H.A., 2006. Swelling of coal in response to CO_2 sequestration
422   for ECBM and its effect on fracture permeability. Spe Journal 11(03), 390-398.
423
424   Mostaghimi, P., Armstrong, R.T., Gerami, A., Hu, Y., Jing, Y., Kamali, F., Liu, M., Liu, Z., Lu, X., Ramandi,
425   H.L. and Zamani, A., 2017. Cleat-scale characterisation of coal: An overview. Journal of Natural Gas
426   Science and Engineering.
427
428   Pentland, C.H., El‑Maghraby, R., Iglauer, S., Blunt, M.J., 2011. Measurements of the capillary trapping
429   of super‑critical carbon dioxide in Berea sandstone. Geophysical Research Letters 38.
430
431   Pillalamarry, M., Harpalani, S. and Liu, S., 2011. Gas diffusion behavior of coal and its impact on
432   production from coalbed methane reservoirs. International Journal of Coal Geology 86(4), 342-348.
433
434   Potyondy, D.O. and Cundall, P.A., 2004. A bonded-particle model for rock. International journal of rock
435   mechanics and mining sciences, 41(8), 1329-1364.
436
437   Saghafi, A., 2010. Potential for ECBM and CO_2 storage in mixed gas Australian coals. International
438   Journal of Coal Geology 82(3), 240-251.
439
440   Sarmadivaleh, M., 2012. Experimental and numerical study of interaction of a pre-existing natural
441   interface and an induced hydraulic fracture. Curtin University.
442
443   Scholtès, L.U.C. and Donzé, F.V., 2012. Modelling progressive failure in fractured rock masses using a
444   3D discrete element method. International Journal of Rock Mechanics and Mining Sciences 52, 18-30.
445

446 Seidle, J., Jeansonne, M., Erickson, D., 1992. Application of matchstick geometry to stress dependent
447 permeability in coals, SPE rocky mountain regional meeting. Society of Petroleum Engineers.
448
449 Sheorey, P., 1994. A theory for in situ stresses in isotropic and transverseley isotropic rock,
450 International journal of rock mechanics and mining sciences & geomechanics abstracts. Elsevier, 23-
451 34.
452
453 Shi, J.Q. and Durucan, S., 2005. A model for changes in coalbed permeability during primary and
454 enhanced methane recovery. SPE Reservoir Evaluation & Engineering 8(04) 291-299.
455
456 Siriwardane, H., Haljasmaa, I., McLendon, R., Irdi, G., Soong, Y. and Bromhal, G., 2009. Influence of
457 carbon dioxide on coal permeability determined by pressure transient methods. International Journal
458 of Coal Geology 77(1), 109-118.
459
460 Tajduś, K., 2009. New method for determining the elastic parameters of rock mass layers in the region
461 of underground mining influence. International Journal of Rock Mechanics and Mining Sciences 46,
462 1296-1305.
463
464 Tu, Q., Cheng, Y., Guo, P., Jiang, J., Wang, L. and Zhang, R., 2016. Experimental study of coal and gas
465 outbursts related to gas-enriched areas. Rock Mechanics and Rock Engineering 49(9), 3769-3781.
466
467 Vialle, S., Lebedev, M., 2015. Heterogeneities in the Elastic Properties of Microporous Carbonate Rocks
468 at the Microscale from Nanoindentation Tests, 2015 SEG Annual Meeting. Society of Exploration
469 Geophysicists.
470
471
472 Vishal, V., Singh, T.N. and Ranjith, P.G., 2015. Influence of sorption time in CO_2-ECBM process in Indian
473 coals using coupled numerical simulation. Fuel *139*, 51-58.
474
475 Wang, T., Zhou, W., Chen, J., Xiao, X., Li, Y., Zhao, X., 2014. Simulation of hydraulic fracturing using
476 particle flow method and application in a coal mine. International Journal of Coal Geology 121, 1-13.
477
478 White, C.M., Smith, D.H., Jones, K.L., Goodman, A.L., Jikich, S.A., LaCount, R.B., DuBose, S.B., Ozdemir,
479 E., Morsi, B.I. and Schroeder, K.T., 2005. Sequestration of carbon dioxide in coal with enhanced
480 coalbed methane recovery a review. Energy & Fuels 19(3), 659-724.
481
482 Wu, Y., Liu, J., Elsworth, D., Siriwardane, H. and Miao, X., 2011. Evolution of coal permeability:
483 Contribution of heterogeneous swelling processes. International Journal of Coal Geology 88(2), 152-
484 162.
485
486 Xu, X., Sarmadivaleh, M., Li, C., Xie, B. and Iglauer, S., 2016. Experimental study on physical structure
487 properties and anisotropic cleat permeability estimation on coal cores from China. Journal of Natural
488 Gas Science and Engineering, 35, 131-143
489
490 Zhai, C., Xiang, X., Xu, J. and Wu, S., 2016. The characteristics and main influencing factors affecting
491 coal and gas outbursts in Chinese Pingdingshan mining region. Natural Hazards, 82(1), 507-530.
492
493 Zhang, Y., Lebedev, M., Sarmadivaleh, M., Barifcani, A., Iglauer, S., 2016a. Change in Geomechanical
494 Properties of Limestone Due to Supercritical CO_2 Injection, SPE Asia Pacific Oil & Gas Conference and
495 Exhibition. Society of Petroleum Engineers.
496

497 Zhang, Y., Lebedev, M., Sarmadivaleh, M., Barifcani, A., Iglauer, S., 2016b. Swelling‑induced changes
498 in coal microstructure due to supercritical CO_2 injection. Geophysical Research Letters 43, 9077-9083.
499
500 Zhang, Y., Lebedev, M., Sarmadivaleh, M., Barifcani, A., Rahman, T., Iglauer, S., 2016c. Swelling effect
501 on coal micro structure and associated permeability reduction. Fuel 182, 568-576.
502
503 Zhang, Y., Xu, X., Lebedev, M., Sarmadivaleh, M., Barifcani, A., Iglauer, S., 2016d. Multi-scale x-ray
504 computed tomography analysis of coal microstructure and permeability changes as a function of
505 effective stress. International Journal of Coal Geology 165, 149-156.
506
507 Zhang, Z., Zhang, G., Li, S., Li, R., Dong, H., Ding, X., 2016e. Modified relationship between point loading
508 strength and uniaxial compressive strength by DEM, 50th US Rock Mechanics/Geomechanics
509 Symposium. American Rock Mechanics Association.
510
511 Zhang, Y., Sarmadivaleh, M., Barifcani, A., Lebedev, M. and Iglauer, S., 2016f. Coal microstructure
512 changes due to water absorption and CO2 injection. The APPEA Journal 56(2), 593-593.
513
514 Zhou, S., Zhu, H., Yan, Z., Ju, J.W., Zhang, L., 2016. A micromechanical study of the breakage
515 mechanism of microcapsules in concrete using PFC2D. Construction and Building Materials 115, 452-
516 463.
517
518 Zhu, W., Fonteyn, M., Hughes, J., Pearce, C., 2009. Nanoindentation study of resin impregnated
519 sandstone and early-age cement paste specimens, Nanotechnology in Construction 3. Springer, 403-
520 408.